Microfluid Nanofluid (2012) 13:499–509
DOI 10.1007/s10404-012-0987-6

RESEARCH PAPER

A microgrooved membrane based gas–liquid contactor

Jigar M. Jani · Matthias Wessling · Rob G. H. Lammertink

Received: 5 January 2012 / Accepted: 11 April 2012 / Published online: 9 May 2012

Abstract This research presents an approach for applying microgrooved membranes for improved gas–liquid contacting. The study involves analysis of the performance of the microdevice by quantifying the flux enhancement for different membrane configurations. Two kinds of configurations, continuous and non-continuous grooves, were investigated. The microgrooves provide shear-free gas–liquid interfaces, which result in local slip velocity at the gas–liquid interface. Exploiting this physical phenomenon, it is possible to reduce mass transport limitations in gas–liquid contacting. An experimental study using grooved membranes suggests enhancement in flux up to 20–30 %. The flux enhancement at higher liquid flow rates is observed due to a partial shear-free gas–liquid interface. The performance of the membrane devices decreased with wetted microgrooves due to the mass transport limitations. The flow visualization experiments reveal wetting of the microgrooves at higher liquid flow rates. According to the numerical and experimental study, we have shown that microgrooved membranes can be employed to improve gas–liquid contacting processes.

Keywords Micropatterned membrane · Slip flow · Flux enhancement · Gas–liquid systems

J. M. Jani · M. Wessling · R. G. H. Lammertink (✉)
Soft Matter, Fluidics and Interfaces, MESA+ Institute for Nanotechnology, University of Twente, Enschede, The Netherlands
e-mail: r.g.h.lammertink@utwente.nl

1 Introduction

Microfluidic systems offer a number of advantages such as enhanced heat and mass transfer intensifying many chemical and biological processes (Hessel et al. 2005; Jensen. 2001; Jähnisch et al. 2004). Numerous studies have been performed regarding multiphase flows (at micro- and nanoscale) for important applications in the field of microfluidic devices (Kreutzer et al. 2005; Heiszwolf et al. 2001; Gervais and Jensen 2006; Shao et al. 2009; Atencia and Beebe 2004; Squires and Quake 2005). The mass transfer limitations present in single-phase flow can be reduced by introducing an additional immiscible fluid. Such multiphase systems induce recirculation motion in the liquid stream that enhanced mixing. An important field of application for these systems considers gas–liquid contacting/reactions (Gunther and Jensen 2006). For gas–liquid reactions, often multiphase systems are employed to achieve fast mixing, lower mass transfer limitations and better control over reaction conditions (Hessel et al. 2005).

The flow behavior at the microscale is considerably different than that in macroscopic flows. The fluid flow at the microscale can be characterized by high surface-to-volume ratios. Due to their characteristic sub-millimeter dimensions (50–500 μm) the flow is mainly laminar ($Re \sim$ 1–100) and mixing proceeds via diffusion dominantly. There have been many attempts to enhance mixing in the microchannel using active and passive micromixers (Stroock et al. 2002; Liu et al. 2002; Stone et al. 2004; Kamholz et al. 1999).

Active mixing can be achieved by creating instabilities in the flow field (Nguyen and Wu. 2005), pressure fluctuations (Fujii et al. 2003), thermal power (Mao et al. 2002), electrokinetic forces (Oddy et al. 2001), and ultrasonic actuation (Yang et al. 2001). Active micromixers have

several disadvantages like using external power and complexity in terms of device fabrication, operation and maintenance. Passive micromixers, on the other hand, utilize no additional power other than the principle pressure drop used for the fluid flow. They accomplish mixing due to formation of flow features induced by geometrical features of the microchannel. One approach to achieve passive mixing is using splitting and recombining which combines two streams flowing from opposite direction (Bothe et al. 2006). Another way of achieving mixing makes use of specifically oriented grooves to generate vortices (Stroock et al. 2002; Bessoth et al. 1999). The twisted microchannels generate curvature induced secondary flows for mixing (Liu et al. 2002;Austinand Seader. 1973; Jiang et al. 2004 Sudarsan and Ugaz 2005 Howell et al. 2004). All these configurations aim for simple yet efficient mixing in the shortest microchannel distance possible.

The flow dynamics along microgrooved superhydrophobic surfaces has been studied extensively (Öner and McCarthy 2000 Torkkeli et al. 2001 Kim and Kim 2002 Bico et al. 2002 Belyaev and Vinogradova 2010; Sbragaglia and Prosperetti 2007;Vinogradova and Belyaev 2011). The frictional resistance offered by such interfaces can be dramatically reduced. The textured surfaces consist of microscale alternating grooves or posts. The hydrophobicity prevents liquid from wetting the grooves and entraps air in the cavity. The gas phase exhibits a much lower viscosity compared to the liquid resulting in interfacial slip velocities (Vinogradova and Belyaev 2011). There has been a lot of work performed, experimentally and numerically, on characterizing this drop in drag using microchannels with superhydrophobic surfaces (Ou et al. 2007; Ou and Rothstein 2005). Sbragaglia and Prosperetti (2007) studied effects of surface deformation caused by pressure difference along the gas–liquid interface, on wetting of superhydrophobic surface consisting of grooves. They also reported a mathematical model that predicts effective slip length for flow conditions with curved gas–liquid interfaces. Maynes et al. (2007) showed experimental and numerical results for laminar flow through a microchannel with superhydrophobic surfaces incorporating grooves aligned parallel to the flow direction. Their numerical predictions showed that the effective slip length increases with increasing relative cavity width and depth. Hassell and Zimmerman (2006) studied numerically the flow through staggered herringbone micromixer (SHM) to characterize the effect of grooves on the fluid flow in the channel for *Re* ranging 0–15. Belyaev and Vinogradova (2010) derived equations describing longitudinal and transverse directional effective slip lengths for various surface slip fractions and orientations.

There are many examples where membranes can be used for gas–liquid contacting utilizing porous hydrophobic membranes (De Jong et al. 2007). Since the gas phase is in contact with the liquid phase along the device, exchange of mass between the two phases is possible. Microgrooves over such membranes gives rise to slip velocities along the gas–liquid interface (Tsai et al. 2009).

As mentioned above, many attempts have been made to achieve lower drag over gas–liquid interfaces using different microgrooved designs. Transport of gas into the liquid using porous membrane microfluidic devices is often limited by small diffusivities of the species involved. The use of microgrooves on hydrophobic surface can be an interesting approach to achieve enhanced transport through porous walls. Here we describe the concept of microgrooved membranes for gas–liquid contacting that allows the investigation of fluid flow and mass transfer in various membrane configurations.

2 Experimental

2.1 Membrane fabrication

The microgrooved membranes studied in this work were fabricated using conventional phase-separation micromolding (Vogelaar et al. 2005) (Fig. 1). Three types of porous PVDF (polyvinylidene fluoride, Hylar 460, and Ausimont) membranes are fabricated for the gas–liquid contacting studies: flat, continuous, and non-continuous (alternated) microgrooved surfaces, as shown in Fig. 1. The silicon wafers were micropatterned through photolithography methods combined with deep reactive ion etching

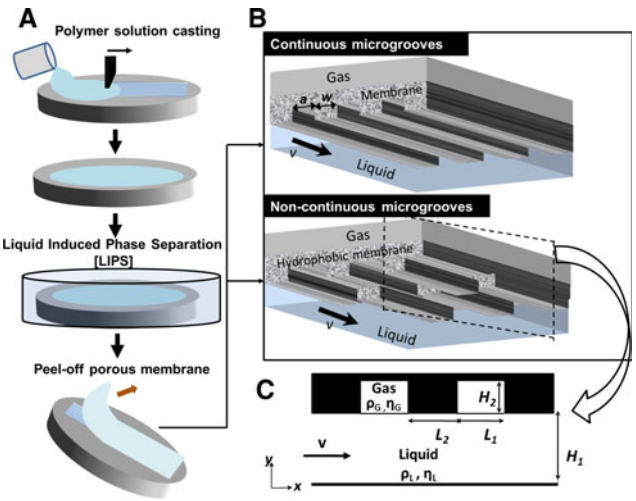

Fig. 1 **a** Schematic representation of phase immersion micromolding to fabricate microgrooves on porous hydrophobic membranes, **b** gas-liquid contacting principle showing liquid flow past continuous and non-continuous microgrooves, **c** geometrical parameters for microgrooved membrane contactor

(DRIE) in cleanroom facilities. Two types of microgrooves were obtained on the molds:

- Mold I: Grooves with a width of 25 μm, a height of 40 μm, a spacing of 75 μm and a length of 50 mm.
- Mold II: as Mold I, but the groove is shifted 50 μm to the side after every 2 mm.

A solution of 20 wt% PVDF in NMP (1-methyl-2-pyrrolidinone, 99 % extra pure, Acros) was prepared by mixing with a mechanical stirrer for 12 h at 70 °C. The polymer solution was then degassed for about 24 h at room temperature. Homogeneous and stable polymer solutions were cast on molds at controlled thicknesses (every 100 μm between 100 and 800 μm). Immediately after casting, the solution together with the microstructured mold was immersed in a coagulation bath consisting of pure ethanol (proanalysis grade, Merck) for 30 min. The membrane separates from the mold after a few minutes. The porous membrane was then taped to a glass plate to prevent it from curling and left to dry in the fume hood overnight. The porous PVDF membrane replicates the microgrooves on the mold. Due to shrinkage during phase separation and drying, the dimensions of the PVDF microchannels are slightly smaller than those on the mold.

2.2 Device fabrication

The porous membranes were incorporated in a gas–liquid contacting module consisting of two poly-methyl methacrylate (PMMA) plates. In these PMMA plates, separate gas and liquid microchannels were created with a CNC-mill (Sherline Inc.). The porous membrane is placed between these plates separating the gas and liquid channel. The liquid channel has a width and depth of 1 mm and a length of 5 cm. The gas channel is made wider and longer on both sides to assure complete coverage of the liquid channel by the porous membrane. Polyether ether ketone (PEEK) tubings (0.75 mm ID) and fittings (0.75 mm ID) from Upchurch Scientific were used for the connections.

2.3 Gas–liquid contacting in various configurations

Uptake of oxygen (obtained from Praxair, Belgium) into demineralized water is chosen as a gas–liquid contacting system (Fig. 2). The setup consists of a programmable syringe pump (Harvard Apparatus, accuracy within 0.35 % and reproducibility within 0.05 %), an oxygen sensor (PreSens Fibox 3, accuracy ±0.15 % air saturation at 1 % air-saturation, resolution 1 ± 0.05 % air-saturation), a mass flow controller (Bronkhorst accuracy ±0.5 % of reading plus ± 0.1 % full scale) and a PC for data acquisition. The gas flow rates were controlled by the mass flow controller and water flow rates by gas-tight syringes using a programmable syringe pump. The feed water was injected at flow rates ranging from 0.05 to 7.5 mL/min ($0.83 < Re < 125$).

The experiments were started by feeding the microchannel with degassed (oxygen-free) water. Water was continuously bubbled with inert nitrogen gas (in a separate vessel) in order to remove the oxygen. Throughout the experiments, the feed water was regularly monitored using

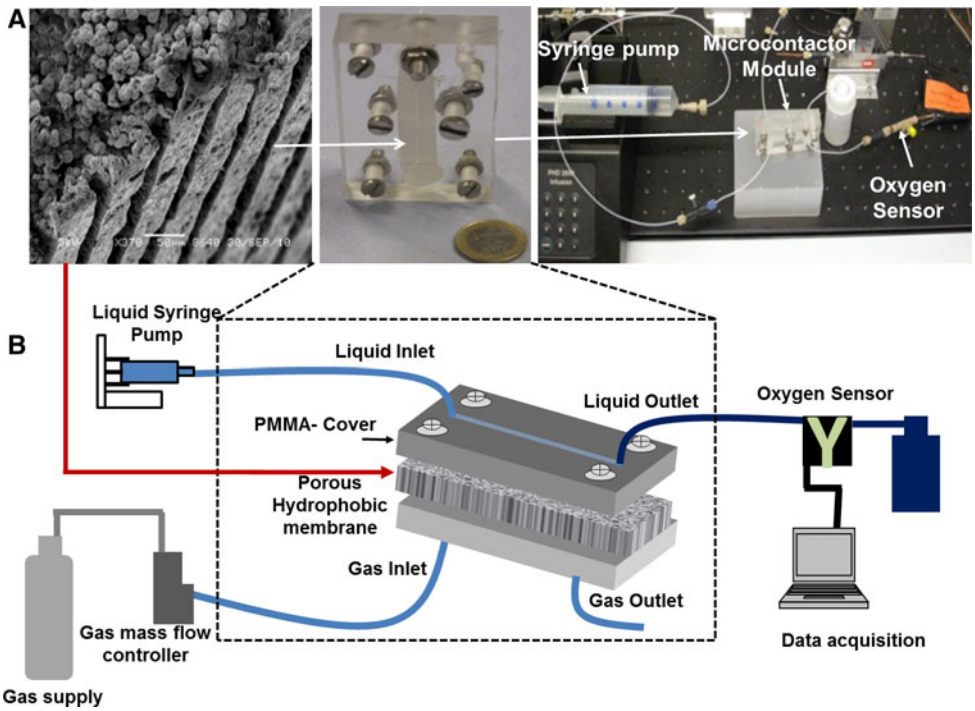

Fig. 2 The gas-liquid contacting experiments. **a** The experiments involves fabrication of microgrooved membranes, incorporating them into the module and setting-up for the gas uptake experiments. These steps are marked with "*arrows*". **b** The schematic representation of experimental set-up used for gas-liquid contacting

the oxygen sensor to verify an oxygen-free inlet. To attain a stable gas–liquid interface during the experiments, the gas was supplied at a fixed pressure and the liquid flow rate was gradually increased until bubbles disappeared at the liquid-side of the microchannel. For higher liquid flow rates, the gas pressure required to establish a well-defined interface also increased. The oxygen concentration was measured for the exiting liquid when steady state was obtained.

The driving force for oxygen transfer varies with the axial position in the module. An expression for the overall oxygen flux at the microchannel outlet, N_o^i, can be expressed by,

$$N_o^i = \int \frac{v_x(y)C(y)\mathrm{d}y}{H_1 W} \tag{1}$$

where, $v_x(y)$ and $C(y)$ are liquid flow rate and oxygen concentration in the liquid, respectively, and N_o^i represents outlet flux for corresponding microfluidic module (flat or microgrooved membrane contactor). Liquid channel height and width are denoted as H_1 and W, respectively. The experiments were carried out at ambient pressure and temperature.

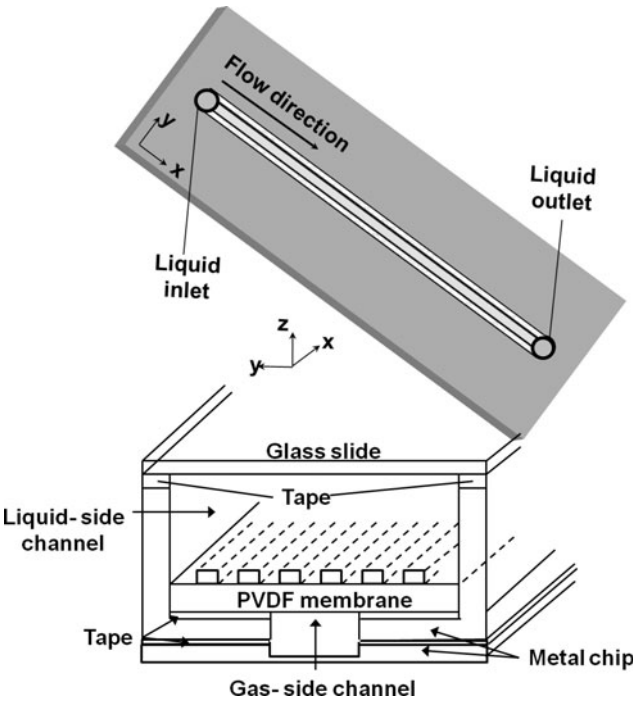

Fig. 3 Illustration of the microfluidic chip used for μPIV and wetting studies at different operating conditions. It shows the stack containing the liquid and gas channel, and a microscopic glass slide for observation

2.4 Characterization

The morphology and dimensions of the porous membrane structures were analyzed by scanning electron microscope (SEM, JSM 5600LV, JEOL). The porous membranes were broken in liquid nitrogen for cross-section analysis. The membrane top surfaces and cross-sections were sputtered with a 30 nm gold layer (SCD040, Balzers Union).

Contact angles of the porous membrane structures are measured with an optical contact angle apparatus (OCA 20, Dataphysics). The water droplet of 5 μL is suspended on the surface with a speed of 2 μm/s. After initial stabilization of the droplet, the contact angle is measured.

An aqueous methylene blue (MB) solution ($\approx$200 mg/L) was prepared and pumped through the liquid inlet for a minimum time of 5 min, in order to visualize the wetting behavior. After that, the membranes were taken out and allowed to dry for 3–4 h and examined by optical microscopy (Zeiss Axiovert 40).

2.5 Micro particle image velocimetry

The microfluidic channel (Fig. 3) was fabricated in a flat metal plate of steel with a depth of 500 μm and 1 mm width. Double sided tape ($\approx$100 μm) was used to bond the PVDF to the steel plate. The PVDF membrane (300 μm) was cut to the width of the module and holes were made for liquid inlet and outlet. Before sealing the microchannel with glass microscopic slide (170 μm) on the ridge of the microfluidic chip, a cut-out in the double sided tape was made to keep the microchannel open. The microscope slide was then placed on the double-sided tape sticking to the chip ridge. The metal chip containing gas-side channel, with inlet and outlet holes, is sticked to the other side of microfluidic channel using double-sided tape.

The module was incorporated in a custom-made holder and connected to the tubing (inner/outer diameter $\approx$0.5/1.6 mm). The module was positioned above the oil immersion Plan-Apochromat 100× objective (numerical aperture NA = 1.4, 1 μm thick local plane) of an inverted optical microscope (Axiovert 40 CFL, Carl Zeiss BV). The oil is halogen-free and low in fluorescence (Immersol 518F, Zeiss). The piezoelectric objective-lens positioning system (MIPOS 500, Piezosystem Jena GmbH) allows for positioning accuracy below 100 nm.

MilliQ water containing fluorescent polystyrene particles with a diameter of 0.3 μm (R300 red fluorescing microspheres, Duke Scientific Corporation) was injected into the microchannel by a syringe pump (PHD 2000, Harvard apparatus GmbH). Liquid flow rates were adjusted in the range of 0.3–17.5 μL/min (Re = 0.008–0.5). Nitrogen gas feed rate was adjusted in the range of 120–220 μL/min corresponding to the changes in the liquid flow rates. A dual-head ND:YLF laser (Pegasus-PIV, New Wave Research) producing green laser pulses with

wavelength 527 nm was used to illuminate the particles. An external pulse delay generator (Model 565, Berkley Nucleonics Corporation) was used to trigger the laser. The time between two pulses is typically 6–15 ms depending on the flow rate. A high-speed charge-coupled device camera (Sensicam, PCO), fit with a 1/2 or 1× lens adapter, was used for imaging. The measurement principle including a sketch of the set-up was described previously (Pirat et al. 2008).

After every measurement 200 image pairs were processed with DaVis imaging software (version 7.2.2.152, LaVision). To obtain time-average velocity profiles, a homemade μPIV post-processing sequence was run in Matlab R2007b (Pirat et al. 2008).

3 Numerical simulation

The momentum and mass balance equations were solved simultaneously under steady-state and laminar flow conditions to study hydrodynamics and mass transport. A three-dimensional model of a straight channel (5 mm long) was considered for flat and microgrooved membranes. The width of the microgroove and microridge are denoted as a and w, respectively. For non-continuous microgrooved membranes, the length and depth of the groove are denoted as L_1 and H_2, the liquid microchannel height is H_1 and the distance between two consecutive grooves (in flow direction) is denoted as L_2. For the numerical simulation, the following properties were considered: the density (ρ_L and ρ_G) and viscosity (η_L and η_G) of the liquid are similar to water and oxygen (1,000 kg m^{-3}, 0.001 Pa s and 1.4 kg m^{-3}, 1 × 10^{-7} Pa s, respectively), a maximum concentration of oxygen in water (saturation point at standard conditions) of 40 mg/L and a diffusion coefficient of oxygen in water of 1.9 × 10^{-9} m^2 s^{-1}.

In order to obtain a mathematically accurate model, the following assumption was made:

1. No mass transfer resistance in the membrane.
2. Flat G–L meniscus for non-wetted condition.
3. Any other forces (gravitational and surface tension forces) are not considered.

The incompressible fluid flow of gas and liquid over a microgrooved membrane is governed by the Navier–Stokes equations:

$$\rho(\boldsymbol{v}\cdot\nabla)\boldsymbol{v} = -\nabla P + \eta\nabla^2\boldsymbol{v} \tag{2}$$

together with the continuity equation:

$$\nabla\cdot\boldsymbol{v} = 0 \tag{3}$$

Here, ρ is the density, P is the pressure, η is the viscosity and $\boldsymbol{v}$ is the velocity vector for the respective phases.

The mass balance equation involving convection and diffusion in the liquid is described as:

$$D\nabla^2 C_L = \boldsymbol{v}\cdot\nabla C_L \tag{4}$$

where D is the diffusion coefficient and C_L is the oxygen concentration in water. The relative importance of diffusion is indicated by the Péclet number, defined as:

$$Pe = \frac{UL}{D} \tag{5}$$

where U, L, and D correspond to the velocity, characteristic length scale, and the diffusion coefficient, respectively. A fully developed laminar flow profile has been implemented at the microchannel inlet and the outlet is kept at normal pressure. There will be zero gas concentration at the microchannel inlet and convective flux will be implemented at the outlet boundary. The microchannel walls (solid–liquid) are "no-slip" boundaries.

$$v_x = v_y = 0, \quad \text{for all solid-liquid interfaces} \tag{6}$$

Along the membrane surface ($y = H_1$), both gas–liquid and liquid–solid interface can apply (depends on continuous or non-continuous microgrooves). A gas–liquid interface is described as a shear-free boundary (velocity of gas and liquid at the interface are equal):

$$v_x = v^i_{x,g} = v^i_{x,l} \tag{7}$$

where $v^i_{x,g}$ and $v^i_{x,l}$ represents gas and liquid interface velocity in x-direction, respectively.

Three-dimensional simulations were performed to investigate the hydrodynamic flow field and mass transport using finite element modeling (COMSOL Multiphysics). The model solves the momentum balance equation (incompressible Navier–Stokes) coupled with the mass balance equation (species convection-diffusion). The numerical results were obtained after performing mesh size dependency analysis. The size of the grid cells for all the 3D models in this study resulted in the range of 0.6–5.8 μm approximately for a mesh density in the range of 37–150 thousand triangular cells (Lagrange type p2,p1) for the total computational domain. The geometrical dimensions of the microgrooves are identical to the observed micropattern dimensions mentioned in Table 1.

Table 1 Dimensions of different features of microgrooved membrane (continuous and non-continuous)

	Mold (μm)	Membrane (μm)	Shrinkage (%)
Groove width	25	24	4
Groove height	40	38	5
Ridge width	75	48	36

4 Results and discussion

4.1 Characterization of the porous membrane

Figure 4 shows the SEM images of the surface and cross-section of the microgrooved membranes. SEM images of various structures in PVDF membranes provide insight in the morphology (i.e., porosity, roughness and porous structure) and dimensions of the membrane microgrooves. The features of the mold are very well represented on the PVDF membranes.

Figure 4a shows the SEM images of flat PVDF membranes in different magnifications. Porous membranes have narrow pore size distribution with average pore size of 7.4 ± 0.7 μm (obtained from SEM images). The membranes are highly porous and contain inter-connected pores. The continuous microgrooved membrane is shown in Fig. 4b, which demonstrates that micropatterns from the mold are nicely replicated in the membranes. A closer look at the structures revealed that the distance between the grooves (50 μm) is slightly smaller than the one on the mold (75 μm). This is due to the shrinkage during the phase inversion process (Vogelaar et al. 2005). Table 1 shows the average values of the dimensions of PVDF membranes.

Compared to Peters (2008), the shrinkage values are found to be somewhat lower and pores have a more open structure. Since all conditions were kept the same except for the coagulation bath (in this work pure ethanol is used instead of 50:50 wt% water:NMP), the differences in the membrane structure are attributed to the phase-separation step. The non-continuous microgrooved membrane can be seen in Fig. 4c. The dimensions of the non-continuous microgrooved membranes are similar to the dimensions of continuous microgrooves.

The water contact angle for the flat membrane was measured to be 128.2 ± 3.4 °. The measured contact angles for these PVDF membranes are higher than previous work from Peters (2008), which is due to the difference in membrane structure.

4.2 Gas uptake in a membrane microcontactor

Figure 5 presents the outlet oxygen concentration for a continuously microgrooved membrane for both experiments

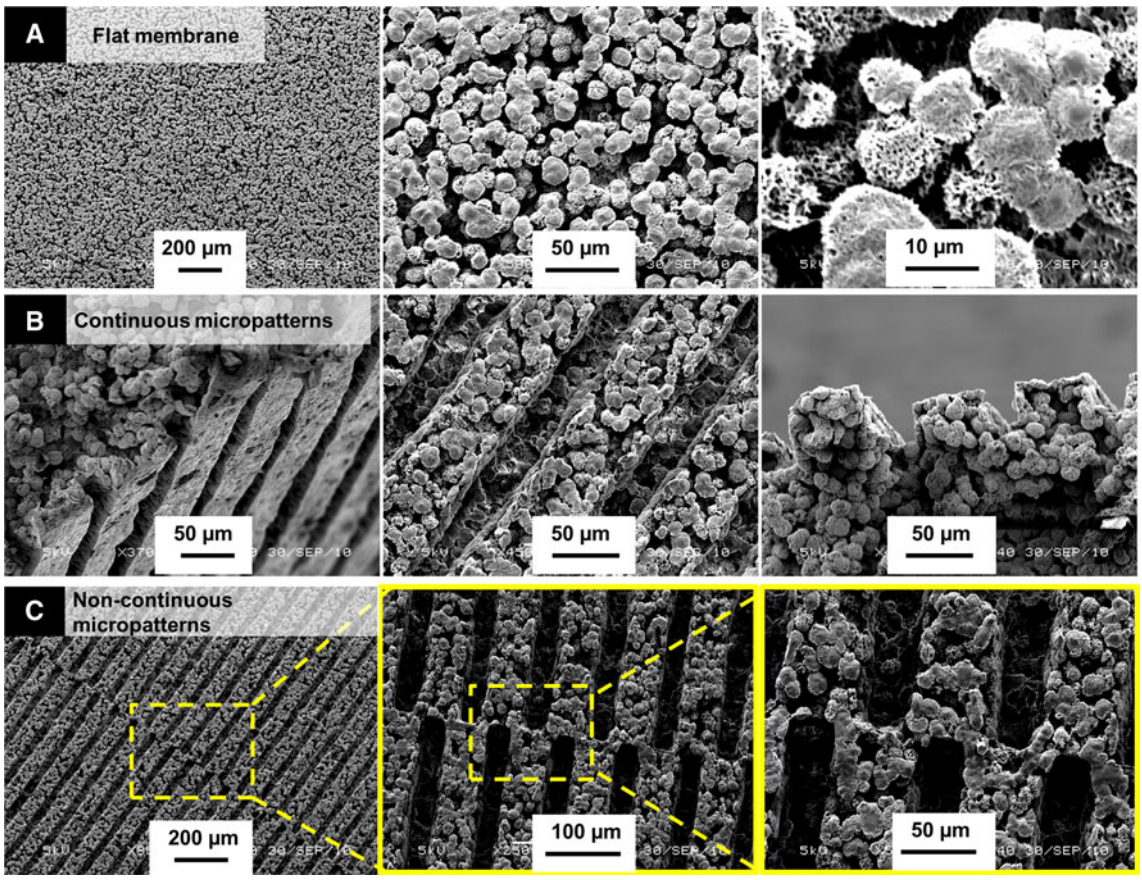

Fig. 4 SEM images of the channels in porous PVDF membrane. **a** Microporous flat PVDF surface. **b** Continuous microgrooved PVDF membrane surface with 24 μm width, 38 μm depth and 48 μm ridge width. **c** Non-continuous microgrooved PVDF membrane surface with 24 μm width, 38 μm depth, 2 mm length and 48 μm ridge width

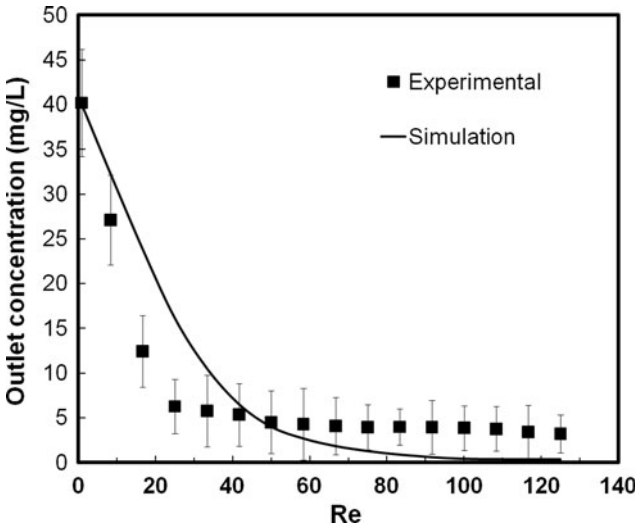

Fig. 5 Outlet oxygen concentration against *Re* for continuous microgrooved membrane module; experimental values are shown in *symbols* and simulation values are shown in *line*

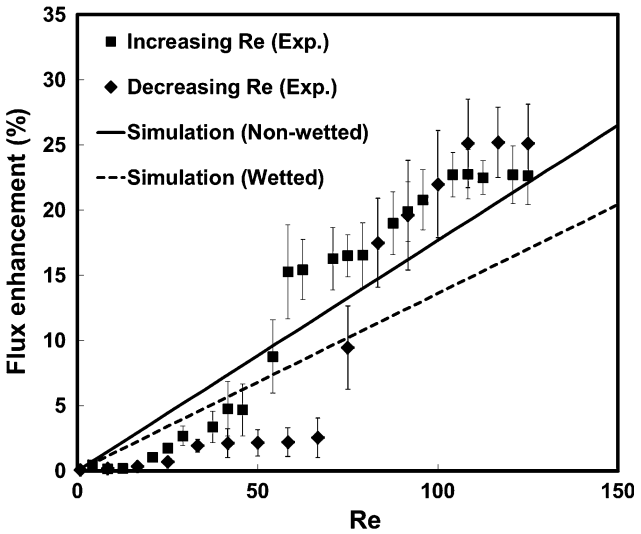

Fig. 6 Flux enhancement versus *Re* for continuous microgrooved membrane module. The values are shown for increasing and decreasing Reynolds number. The experimental values are shown in *dots* and simulation values are shown in *line*

and simulations (oxygen saturation concentration is 40 mg/L at 25 °C and 1 bar). For low *Re* (below 5), the liquid gets saturated almost completely. The measured oxygen concentrations were slightly different compared to the simulated concentrations at high and low liquid flow rates. These differences are due to the experimental error caused by the oxygen sensor sensitivity.

The measured oxygen uptake when using flat and microgrooved membranes allow to calculate the flux enhancement (E):

$$E = \frac{(N_o^m - N_o^f)}{N_o^f} \tag{8}$$

where N_o^m and N_o^f are the outlet flux for microgrooved and flat membrane, respectively.

The flux enhancement for a continuous microgrooved membrane compared to a flat membrane is shown in Fig. 6. The results, both from the numerical model and oxygen absorption experiments, show higher oxygen absorption for the microgrooved membrane compared to the flat membrane. It can be seen from the plot that the experimental flux enhancement increases sharply after $Re = 50$. This increase in flux enhancement can be explained due to enhanced mass transfer caused by an increased gas–liquid interface velocity (slip condition). The numerical results also show reasonable agreement with the experimental observations.

Interestingly, during subsequent decreasing *Re* experiments, hysteresis was observed. The flux enhancement was much lower for *Re* in the range of 50 to 75. The hysteresis could be explained by wetting of the grooves at higher Reynolds number. This causes a change in the oxygen diffusion length and consequently reduces the oxygen mass transfer rate. The influence of microgroove wetting on the performance of the membrane module was studied numerically as well (Fig. 6). The numerical simulation results display a reduced flux enhancement (for $Re \geq 50$) due to wetting of the grooves.

Figure 7 illustrates the flux enhancement for a non-continuous and a continuous microgrooved membrane. The enhancement in flux for non-continuous grooves is approximately 20–30 % for Reynolds number higher than 75. Due to perturbations in the shear-free interface velocity, displacements perpendicular to the flow direction appear. These

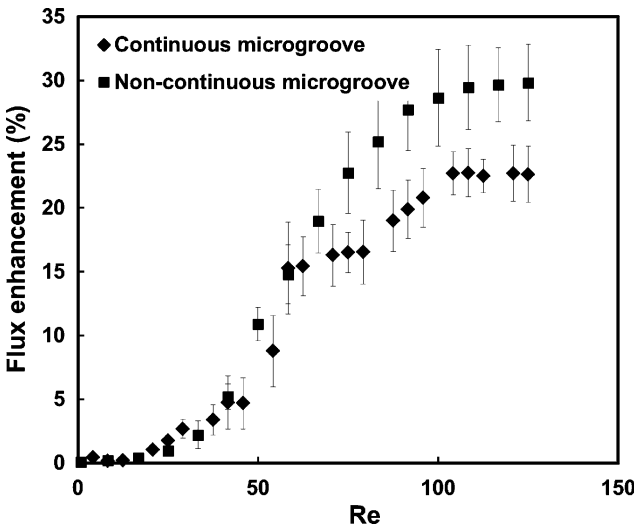

Fig. 7 Flux enhancement versus *Re* for continuous and non-continuous microgrooved membrane module. The values are shown for increasing Reynolds number

displacements generate convective flow near the gas absorbing porous wall, which leads to enhanced gas uptake compared to a continuously microgrooved membrane.

4.3 Details of the gas-liquid interface

Non-wetted grooves give rise to local slip velocities and to validate results with analytical model (Philip 1972), we have to consider two important geometric parameters for the different configurations: the microgroove width (a) and microridge width (w). The cavity fraction is represented by a/d (shown in Fig. 1), where $d = a + w$. Philip showed that for fully developed laminar flow through a parallel-plate channel and with a vanishing shear-stress at the gas-liquid interface, the slip-length, b, can be expressed as:

$$\frac{b}{d} = \frac{1}{\pi} ln \left[\frac{1}{cos\left(\frac{a}{d}\frac{\pi}{2}\right)} \right] \tag{9}$$

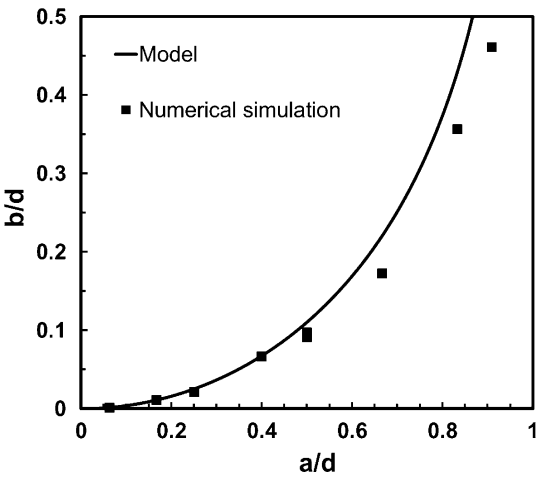

Fig. 8 Numerical results showing values of dimensionless slip length b/d as a function of the dimensionless microgroove width. The results are compared with the analytical expression for b/d, from literature (Philip 1972) represented by Eq. (9)

With Eq. (9), it is possible to quantify slip-length characteristics with a single curve, which allows validation of our numerical results for the limiting case of zero shear-stress at the gas-liquid interface.

The overall shear stress at the gas-liquid interface is strongly dependent on the ridge and groove widths. The effective slip length is calculated from the numerical results and plotted against the microgroove width (Fig. 8). The analytic solution of Philip given by Eq. (9) is also presented. The numerical results show very good agreement with the solution from Philip, not surprisingly as both assume a flat gas-liquid meniscus. However, for high a/d, there is little deviation (lower values than analytical model) of slip length from Philip's formula which can be due to violation of a perfect slip assumption. This can further be validated from the previous work of Belyaev and Vinogradova (Belyaev and Vinogradova, 2010) that shows decreasing effective slip lengths when local slip becomes on the order of the groove period.

To investigate the oxygen absorption in water using different membranes (continuous and non-continuous microgrooves), numerical simulations were performed at flow rates ranging from $0.83 < Re < 125$. The oxygen concentration and fluid flows were investigated to verify our experimental observations. Two different cases were considered: wetted and non-wetted under different flow conditions.

The outlet oxygen concentration vary with the liquid flow rate due to changes in the Péclet number. Typical numerical simulation results for continuous microgrooved membranes, with and without wetting are shown in Fig. 9. In the wetted microgrooves, the average velocity can be calculated from the velocity profile and it is required to determine Pe for various inlet Re. For Re = 0.83 (0.05 μL/min) and 125 (17.5 μL/min), values of Pe are 0.24 and 0.11, respectively, which suggests wetted microgrooves offer mass transfer resistance to oxygen uptake in water.

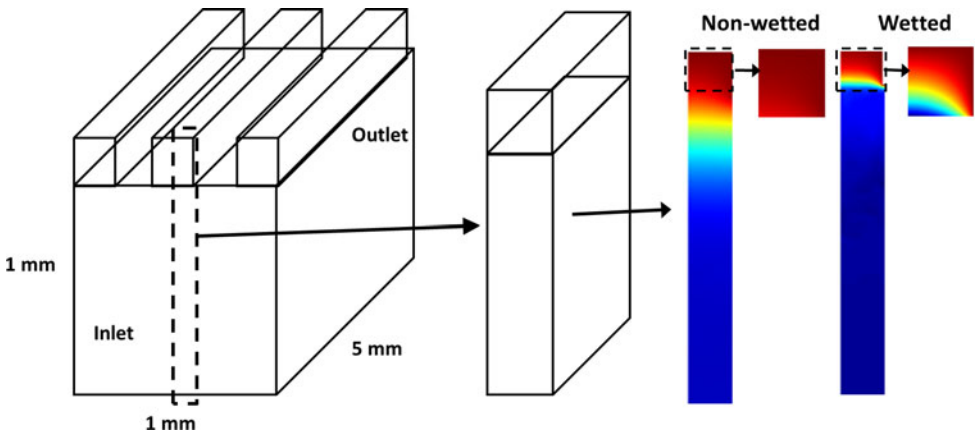

Fig. 9 The numerical simulations showing concentration profiles in a channel with two test cases: wetted and non-wetted mode (Re = 25, D = 1.9 × 10^{-9} m^2/s for 25 μm groove width and 40 μm groove height). The oxygen concentration in the microgrooves is shown in selected *inset images*

4.4 Flow along microgrooved membranes

To investigate the effect of the liquid flow rate on the membrane microgroove wetting, an aqueous methylene blue (MB) solution was pumped through the microchannel for 5 min with increasing flow rates. After every step change in flow rate, the MB stained membrane was taken out and observed by optical microscopy (Fig. 10). The same procedure was followed for decreasing Reynolds numbers.

As shown in Fig. 10 a and c, the water flowing above the microgrooves remains in the Cassie-Baxter state for low flow rates where the differential pressure across the gas-liquid interface has not reached the wetting pressure. However, when the differential pressure exceeds the wetting pressure, water penetrates into the grooves (Wenzel state) (Fig. 10b, d). The observation of water wetting the grooves explains the hysteresis behavior in flux enhancement.

Micro-PIV measurements were performed at liquid flow rates ranging from 0.3-17.5 μL/min ($0.008 < Re < 0.5$). These conditions resulted in completely non-wetted and wetted grooves for lower and higher flow rates, respectively. Figures 11a and b show the plots containing information about the velocity profiles for two different flow rates (5 and 17.5 μL/min) at the same observation plane (5 μm from the micropattern ridge). For low liquid flow rates (Fig. 11a), the grooves are gas filled and a shear-free interface is realized giving enhanced liquid velocity.

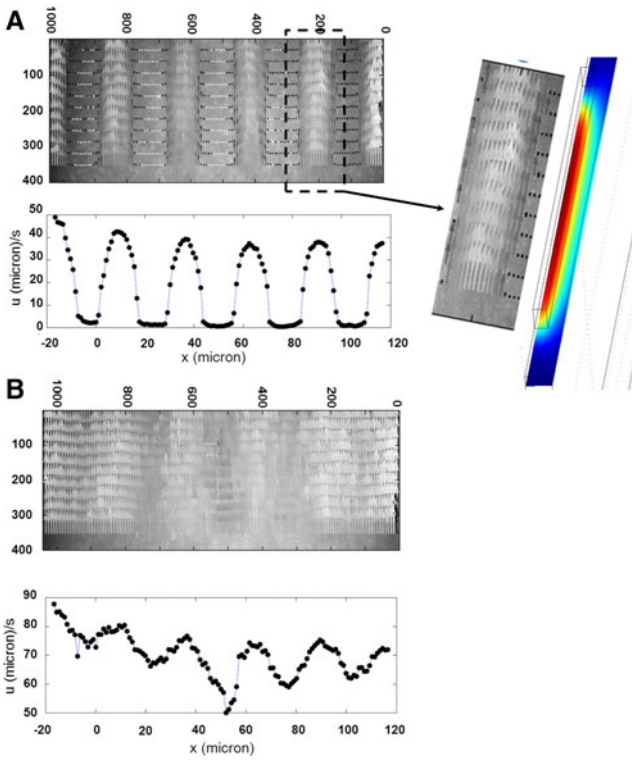

Fig. 11 **a** MicroPIV results showing one frame visualizing the flow (5 μL/min) over a microgrooved PVDF membrane surface at a height $z = 5$ μm from the microgroove ridge (*top*) and the time- and space-averaged velocities in x-direction extracted from this (*bottom*). **b** Particle velocity profile at a flow rate of 17.5 μL/min showing little difference in water velocity over microgrooves and microridges (*top*) and time- and space-averaged velocities (*bottom*)

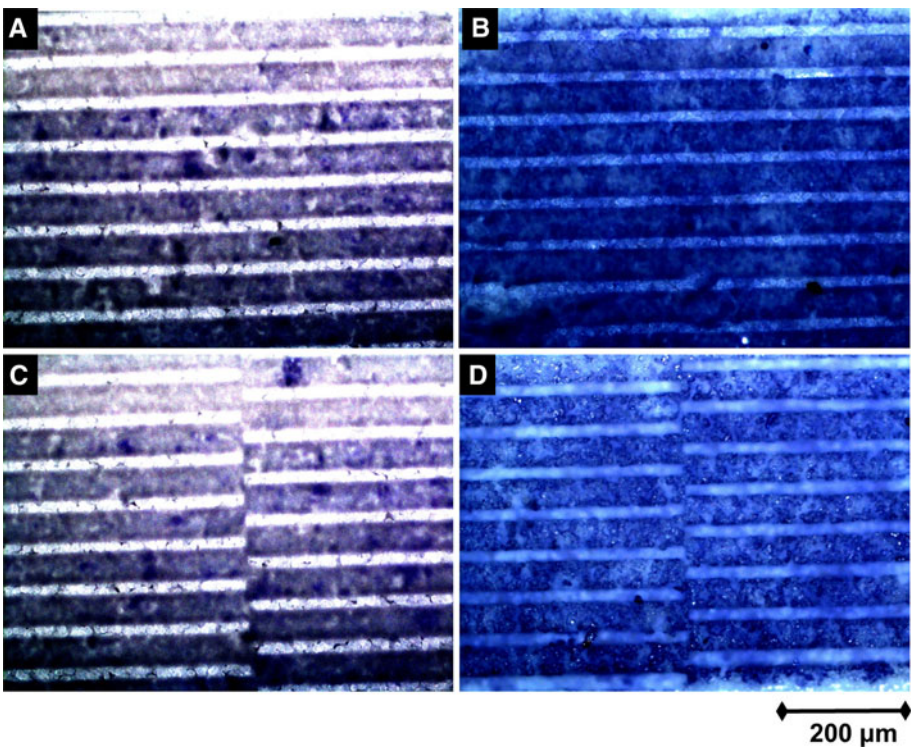

Fig. 10 Optical microscope images of the membranes showing wetting of the grooves. **a** Continuous grooves at low liquid flow rate ($Re = 8.30$) showing liquid remaining in the non-wetted (Cassie-Baxter) state. **b** Continuous grooves at high liquid flow rate ($Re = 120.83$) showing wetting of the grooves. **c** Non-continuous microgrooved membrane surface with low liquid flow rate ($Re = 8.30$). **d** Non-continuous microgrooved membrane surface with high liquid flow rate ($Re = 120.83$) showing wetting of the grooves

Figure 11a (bottom) shows the averaged velocity in x-direction for each position along the y-axis ($v_x(y)$) at a given height z (5 μm). It displays near zero liquid velocity above the microgroove ridge and a liquid velocity of 40 μm/s above the gas filled groove.

The velocity of water flowing over wetted microgrooves (Fig. 11b) is not significantly higher than the velocity of water flowing over microridges. The completely wetted membrane surface (Wenzel state) is also observed during the experiments. The higher averaged liquid velocity (Fig. 11b bottom) is observed due to the higher liquid flow rate.

5 Conclusions

The main goal of this work was to design a microgrooved membrane for gas-liquid contacting that was easy to fabricate, efficient and simple. This work presents a system which can be employed in effective gas-liquid contacting. By this approach, it is possible to reduce the mass transport limitations commonly observed in conventional gas-liquid contacting system. An enhancement in flux up to 20–30 % has been observed. The liquid flow patterns and wetting behavior of the porous microgrooved hydrophobic membranes have been analysed experimentally and numerically. The flux in grooved membrane is enhanced at higher liquid flow rates due to slip flow at the gas-liquid interface. However when the microgrooves are wetted the mass transport decreases. Microgrooved membranes offer a promising alternative to conventional membranes because of a significant enhancement in constituent transport. The experiments also show the limits of the flow regimes characterized by observing the position of gas-liquid interface. According to both the numerical simulations and experimental observations of gas-liquid contacting, we have shown that it is possible to increase the gas uptake by merely structuring the membrane surface.

Acknowledgments This work was financially supported by Stichting voor de Technische Wetenschappen (STW, Project 07569) in The Netherlands. The authors also greatly acknowledge Elif Karatay (SFI/TNW) for mold preparation and Alvaro Gomez Marin (POF/TNW) for μPIV analysis and technical support.

References

Atencia J, Beebe D (2004) Controlled microfluidic interfaces. Nat Biotechnol 437(7059):648–655

Austin L, Seader J (1973) Fully developed viscous flow in coiled circular pipes. AIChE J 19(1):85–94

Belyaev A, Vinogradova O (2010) Effective slip in pressure-driven flow past super-hydrophobic stripes. J Fluid Mech 652: 489–499

Bessoth F, deMello A, Manz A (1999) Microstructure for efficient continuous flow mixing. Anal Commun 36(6):213–215

Bico J, Thiele U, Quéré D (2002) Wetting of textured surfaces. Colloids Surf, A 206(1–3):41–46

Bothe D, Stemich C, Warnecke H (2006) Fluid mixing in a T-shaped micro-mixer. Chem Eng Sci 61(9):2950–2958

De Jong J, Geerken M, Lammertink R, Wessling M (2007) Porous microfluidic devices–fabrication and applications. Chem Eng Technol 30(3):309–315

Fujii T, Sando Y, Higashino K, Fujii Y (2003) A plug and play microfluidic device. Lab Chip 3(3):193–197

Gervais T, Jensen K (2006) Mass transport and surface reactions in microfluidic systems. Chem Eng Sci 61(4):1102–1121

Gunther A, Jensen K (2006) Multiphase microfluidics: from flow characteristics to chemical and materials synthesis. Lab Chip 6(12):1487–1503

Hassell D, Zimmerman W (2006) Investigation of the convective motion through a staggered herringbone micromixer at low reynolds number flow. Chem Eng Sci 61(9):2977–2985

Heiszwolf J, Kreutzer M, van den Eijnden M, Kapteijn F, Moulijn J (2001) Gas-liquid mass transfer of aqueous taylor flow in monoliths. Catal Today 69(1-4):51–55

Hessel V, Angeli P, Gavriilidis A, Löwe H (2005) Gas-liquid and gas-liquid-solid microstructured reactors: contacting principles and applications. Ind Eng Chem Res 44(25):9750–9769

Hessel V, Löwe H, Schönfeld F (2005) Micromixers: a review on passive and active mixing principles. Chem Eng Sci 60:2479–2501

Howell P, Mott D, Golden J, Ligler F (2004) Design and evaluation of a Dean vortex-based micromixer. Lab Chip 4:663–669

Jähnisch K, Hessel V, Löwe H, Baerns M (2004) Chemistry in microstructured reactors. Angew Chem Int Ed 43(4):406–446

Jensen K (2001) Microreaction engineering—is small better. Chem Eng Sci 56(2):293–303

Jiang F, Drese K, Hardt S, Küpper M, Schönfeld F (2004) Helical flows and chaotic mixing in curved micro channels. AIChE J 50(9):2297–2305

Kamholz A, Weigl B, Finlayson B, Yager P (1999) Quantitative analysis of molecular interaction in a microfluidic channel: the T-sensor. Anal Chem 71(23):5340–5347

Kim J, Kim C (2002) Nanostructured surfaces for dramatic reduction of flow resistance in droplet-based microfluidics. In: Micro Electro Mechanical Systems, 2002. The Fifteenth IEEE International Conference on IEEE, pp 479–482

Kreutzer M, Kapteijn F, Moulijn J, Kleijn C, Heiszwolf J (2005) Inertial and interfacial effects on pressure drop of taylor flow in capillaries. AIChE J 51(9):2428–2440

Liu R, Stremler M, Sharp K, Olsen M, Santiago J, Adrian R, Aref H, Beebe D (2002) Passive mixing in a three-dimensional serpentine microchannel. J Microelectromech Syst 9(2):190–197

Mao H, Yang T, Cremer P (2002) A microfluidic device with a linear temperature gradient for parallel and combinatorial measurements. J Am Chem Soc 124(16):4432–4435

Maynes D, Jeffs K, Woolford B, Webb B (2007) Laminar flow in a microchannel with hydrophobic surface patterned microribs oriented parallel to the flow direction. Phys Fluids 19:093,603

Nguyen N, Wu Z (2005) Micromixers-a review. J Micromech Microeng 15:R1

Oddy M, Santiago J, Mikkelsen J (2001) Electrokinetic instability micromixing. Anal Chem 73(24):5822–5832

Öner D, McCarthy T (2000) Ultrahydrophobic surfaces. Effects of topography length scales on wettability. Langmuir 16(20):7777–7782

Ou J, Rothstein J (2005) Direct velocity measurements of the flow past drag-reducing ultrahydrophobic surfaces. Phys Fluids 17:103–606

Ou J, Moss G, Rothstein J (2007) Enhanced mixing in laminar flows using ultrahydrophobic surfaces. Phys Rev E 76(1):16–304

Peters A (2008) Micro-patterned interfaces affecting transport through and along membranes. PhD thesis

Philip J (1972) Flows satisfying mixed no-slip and no-shear conditions. Zeitschrift für Angewandte Mathematik und Physik (ZAMP) 23(3):353–372

Pirat C, Naso A, Van Der Wouden E, Gardeniers J, Lohse D, Van Den Berg A (2008) Quantification of electrical field-induced flow reversal in a microchannel. Lab Chip 8(6):945–949

Sbragaglia M, Prosperetti A (2007) A note on the effective slip properties for microchannel flows with ultrahydrophobic surfaces. Phys Fluids 19:043–603

Shao N, Gavriilidis A, Angeli P (2009) Flow regimes for adiabatic gas-liquid flow in microchannels. Chem Eng Sci 64(11): 2749–2761

Squires T, Quake S (2005) Microfluidics: Fluid physics at the nanoliter scale. Rev Mod Phys 77(3):977

Stone H, Stroock A, Ajdari A (2004) Engineering flows in small devices. Annu Rev Fluid Mech 36:381–411

Stroock A, Dertinger S, Ajdari A, Mezić I, Stone H, Whitesides G (2002) Chaotic mixer for microchannels. Sci Agric 295(5555):647

Sudarsan A, Ugaz V (2005) Fluid mixing in planar spiral microchannels. Lab Chip 6(1):74–82

Torkkeli A, Saarilahti J, Haara A, Harma H, Soukka T, Tolonen P (2001) Electrostatic transportation of water droplets on superhydrophobic surfaces. In: Micro Electro Mechanical Systems, 2001 (MEMS 2001). The 14th IEEE International Conference on IEEE, pp 475–478

Tsai P, Peters A, Pirat C, Wessling M, Lammertink R, Lohse D (2009) Quantifying effective slip length over micropatterned hydrophobic surfaces. Phys Fluids 21:112–002

Vinogradova O, Belyaev A (2011) Wetting, roughness and flow boundary conditions. J Phys: Condens Matter 23:184–104

Vogelaar L, Lammertink R, Barsema J, Nijdam W, Bolhuis-Versteeg L, Van Rijn C, Wessling M (2005) Phase separation micromolding: a new generic approach for microstructuring various materials. Small Bus Econ 1(6):645–655

Yang Z, Matsumoto S, Goto H, Matsumoto M, Maeda R (2001) Ultrasonic micromixer for microfluidic systems. Sens Actuators A Phys 93(3):266–272